Journal of Applied Fluid Mechanics, Vol. 11, No. 2, pp. 343-352, 2018.
Available online at www.jafmonline.net, ISSN 1735-3572, EISSN 1735-3645.
DOI: 10.29252/jafm.11.02.28302

The Effects of the Reynolds Number on the Hydrodynamics Characteristics of an AUV

K. Mostafapour, N. M. Nouri† and M. Zeinali

School of Mechanical Engineering, Iran University of Science and Technology, Tehran, Iran

†*Corresponding Author Email: mnouri@iust.ac.ir*

(Received August 9, 2017; accepted October 21, 2017)

ABSTRACT

The hydrodynamic characteristics of autonomous underwater vehicles (AUVs) play a significant role in the design and analysis of their maneuverability. This paper evaluates the effects of the Reynolds (Re) number on the hydrodynamic characteristics of AUV for various angles of attack (AOA). To estimate the hydrodynamic parameters, a numerical modelling based on computational fluid dynamics (CFD) is employed. Reynolds numbers between 2×10^6 and 150×10^6 were examined at -10º to 10º AOAs. Experimental tests for the same AUV in Re = 2×10^6 in the water tunnel were carried out for CFD validation. A comparison of the results showed an acceptable agreement between the numerical method and the experimental results. The results show that hydrodynamic parameters can be a function of Re and converge on a constant in a limited value when the Re number increases. Results of independent parameters, can be used for full-scale without the establishment of dynamic similarity.

Keywords: Hydrodynamic characteristics; AUV; CFD; Water tunnel.

NOMENCLATURE

A	angle of attack
$C_{1\varepsilon}, C_{2\varepsilon}, C_{\mu}$	turbulence constants
C_{Dp}	pressure drag coefficient
C_{Df}	frictional drag coefficient
C_D	drag coefficient
C_L	lift coefficient
C_M	moment coefficient
A	cross section area
d	body diameter
ρ	fluid density
U	free flow velocity
k	turbulent kinetic energy
l	model length
L	lift force
M	moment about *y*-axis
M_w	linear hydrodynamic coefficient of heave moment
$M_{w\|w\|}$	nonlinear hydrodynamic coefficient of heave moment
P	Reynolds-averaged pressure
Re	Reynolds number
U	model velocity
$\dot{u}$	acceleration the x direction
U_i, U_j	mean velocity components of fluid
u_i, u_j	fluctuation velocity components of fluid
y^+	non-dimensional distance of the first node near to the wall
Z	force the z direction
Z_w	linear hydrodynamic coefficient of heave force
$Z_{w\|w\|}$	nonlinear coefficient of force as functions of heave velocity
ε	viscous dissipation rate of turbulent kinetic energy
μ	fluid dynamic viscosity
μ_t	eddy viscosity
ρ	flow density
$\sigma_k, \sigma_\varepsilon$	turbulence prantl number for k and ε

1. INTRODUCTION

Due to the increasing applications of AUVs for underwater explorations, hydrographic survey, and defensive operations in recent years, the research and development of AUVs have drawn great attention. All design aspects, including hydrodynamic performance, should be fully considered due to the complications and changes occurring in their operation settings. Designing submarine vehicles for low drag and good handling and stability has been the major topic of many recent studies. One challenging problem in efficiently designing AUVs for different operating conditions is to know the accurate hydrodynamic parameters. The unavailability of a reliable model to use to estimate the drag and hydrodynamic parameters for incompressible flows with possible separation can be a reason for this problem. In addition, the flow physics in the boundary-layer transition region, the boundary layer turbulent region, the turbulence boundary layer separation region, and the wake region of separation are not yet fully understood. All these aspects are primarily important when anticipating hydrodynamic parameters. The referred factors can be a function of the Re number and the AOAs. Any change in the Re number may negatively influence the hydrodynamic parameters, including the lift and drag coefficients at different AOAs and the hydrodynamic derivatives.

The hydrodynamic parameters are applied to designing the AUV hull and determining speed-related derivatives. Hydrodynamic characteristics of the AUVs' speeds have been widely studied in recent years. Sarkar *et al.* (1997) evaluated the performance of k-ε turbulence models by two-dimensionally simulating different submarine objects at zero AOA. Bellevre *et al.* (2001) used a translational and rotational model based on Reynolds Averaged Navier-Stokes (RANS) in a steady state to estimate the speed-related hydrodynamic derivatives. Results obtained by the hydrodynamic model were in good agreement with the empirical data. Wu *et al.* (2005) simulated the steady straight line of the SUBOFF model with or without the angle of attack for the model close to the infinite level bottom. Here, the effects of the motion-near-bottom on the hydrodynamic forces were evaluated. Using the RANS solvers, Tyagi and Sen (2006) measured the transverse speed-related coefficients. Phillips *et al.* (2007) reported a set of calculation approaches used to predict hydrodynamic coefficients for different sway speeds. In their studies, they used different numerical strategies, including a dsrift test and a rotating arm test to estimate the submarine hull coefficients. Barros *et al.* (2008) developed numerical techniques to estimate the force and moment characteristics of the underwater hulls in various AOAs. The findings obtained by CFD were compared with semi- and empirical results. Jagadeesh *et al.* (2009) conducted a comparative evaluation between experimental and numerical studies. Lift and drag coefficients were estimated for AOAs at 0 to 15. Hussani *et al.* (2009) made an effort to study the effect of drag on co-operative AUV motions with the configurations of one leader- one follower under in-line and one-leader-two followers in triangular configurations. They concluded that one leader-one follower in-line will have less drag. Zhang *et al.* (2010) proposed a new method using FLUENT CFD to simulate the hydrodynamic coefficient tests. He then used calculated hydrodynamic coefficients to develop a hydrodynamic model. Using FLUENT CFD, Kim *et al.* (2011) estimated the control coefficients for a high-speed submarine with a cross-shaped tail. Jagadeesh *et al.* (2011) evaluated the general drag and the drag changes in limited Reynolds over co-operative AUV motions at zero AOA for two configurations of one leader-one follower under inline (1L1F - Inline) and one leader-one follower under a staggered state (1L1F-Staggered). Rattanasiri *et al.* (2014) used three general optimization algorithms and three simple drag anticipations based on potential flow method. Du *et al.* (2014) studied the effects of AUV distance from the sea bottom on hydrodynamic characteristics in different AOAs. Mansoorzadeh and Javanmard (2014) assessed the free surface effects on lift and drag coefficients, applying two experimental and numerical methods. Depending on Reynolds can lead to a difference between the values obtained from model tests and the real values required for operating conditions of the AUV hull. The difference- related error can be an effective factor for accurately estimating hydrodynamic parameters to be used in the designing process and for controlling AUV.

Considering these physical factors, this paper evaluates the effects of the Reynolds number on the drag and lift coefficients at different angles of attack (AOA) and speed-related linear and nonlinear hydrodynamic derivatives. To estimate the hydrodynamic parameters, a numerical modeling based on computational fluid dynamics (CFD) is presented. Similar experimental tests were carried out to validate the proposed model in a water tunnel.

2. THE AUV MODEL AND ITS HYDRODYNAMIC CHARACTERESTICS

The HydroLab 500 is an AUV with an optimum design developed and constructed to do research at the Iran University of Science and Technology. In the hydrodynamic design, some requirements, including non-separation, non-cavitation, and minimization of fluid resistant force were considered. Figure 1 shows the HydroLab 500. The HydroLab 500 is controlled by four wings located in across shape at the endpoint of the body.

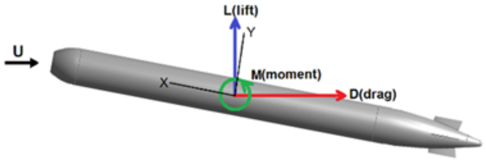

Fig. 1. HydroLab 500 AUV.

Shear stress and pressure distribution produce hydrodynamic forces and moments over the AUV surface. The resulting force is divided into lift (L) and drag (D) forces that are parallel and perpendicular to the free flow velocity, respectively. Drag, lift, and moment (M) coefficients are equal to:

$$C_D = \frac{D}{\frac{1}{2}\rho U^2 A}, \tag{1}$$

$$C_L = \frac{L}{\frac{1}{2}\rho U^2 A}, \tag{2}$$

$$C_M = \frac{M}{\frac{1}{2}\rho U^2 l^3}, \tag{3}$$

where $A = \frac{\pi d^2}{4}$, ρ is density, l is length, and U is the free flow velocity. The force imposed on the body in the direction perpendicular to the longitudinal axis is equal to:

$$Z = D\sin\alpha + L\cos\alpha, \tag{4}$$

where α is the carrying angle between the velocity and the longitudinal axis of the body. The squared absolute fit was used to estimate derivatives from the calculated forces and moments as:

$$Z' = Z'_{w'}w' + Z_{w'|w'|}w'|w'|, \tag{5}$$

$$M' = M'_{w'}w' + M'_{w'|w'|}w'|w'|, \tag{6}$$

where $w' = \sin\alpha = \frac{w}{U}$, Z' is the non-dimensional force ($\frac{Z}{\frac{1}{2}\rho U^2 l^2}$) imposed on the body in the direction perpendicular to the longitudinal axis. M' is the non-dimensional moment ($\frac{M}{\frac{1}{2}\rho U^2 l^3}$) about some reference point on the body. Note that the non-dimensional moment M' is same as C_M. Using Eq. (4) the non-dimensional force Z' can be calculated from the computed values of drag and lift coefficients at various angles of attack. The angle of attack was defined as the angle between velocity and longitudinal axis of the body. Using a curve-fitting approximation suitable for the calculated data, the coefficients of $Z'_{w'}$, $Z_{w'|w'|}$, $M'_{w'}$ and $M'_{w'|w'|}$ are estimated. These coefficients are applied to the estimation of AUV velocity-related forces and moments in dynamic equations.

3. NUMERICAL PROCEDURE

3.1 The Mathematical Equations

Resolving the flow around the model is based on RANS. Assuming the fluid as incompressible, the flow equations are as follows:

$$\left(\frac{\partial U}{\partial t}\right) + \nabla.(\nabla U) = -\frac{1}{\rho}\nabla P + \frac{\mu}{\rho}\nabla.(\nabla U + \nabla U^T) + \frac{1}{\rho}\nabla(-\overline{u'u'}), \tag{7}$$

$$\nabla.U = 0 \tag{8}$$

Where ρ is density and P is the Reynolds-averaged pressure. U and u refer to the fluid mean and fluctuation velocity components, respectively. μ is the fluid dynamic viscosity and $\overline{u'u'} = \overline{u'_i u'_j}$ indicates fluid Reynolds stresses. Hydrolab 500 AUV designed and developed in Iran University of Science and Technology (IUST) for applications in the deep sea. Thus, the effects of surface waves on AUVs related to gravitational force were negligible. In the numerical simulations, gravitational forces of the model were eliminated to estimate the pure hydrodynamic forces and moments. $k-\varepsilon$ is the turbulence model applied to calculate the Reynolds stresses. $k-\varepsilon$ is one of the most commonly used models in aerodynamic and hydrodynamic flows. The $k-\varepsilon$ equations are as follows:

$$\frac{\partial}{\partial t}(\rho k) + \nabla.(\rho k U) = \nabla.\left[\left(\mu + \frac{\mu_t}{\sigma_k}\right)\nabla k\right] + P_k - \rho\varepsilon, \tag{9}$$

$$\frac{\partial}{\partial t}(\rho\varepsilon) + \nabla.(\rho\varepsilon U) = \nabla.\left[\left(\mu + \frac{\mu_t}{\sigma_\varepsilon}\right)\nabla\varepsilon\right] + \frac{\varepsilon}{k_t}(C_{1\varepsilon}P_k - C_{1\varepsilon}\rho\varepsilon), \tag{10}$$

where,

$$P_k = \mu_t \nabla U.(\nabla U + \nabla U^T) + \frac{2}{3}\nabla.U[3\mu_t \nabla.U + \rho k)], \tag{11}$$

$$\mu_t = C_\mu \rho \frac{k^2}{\varepsilon}. \tag{12}$$

In the above equations k is the turbulent kinetic energy, and ε implies the viscous dissipation rate of turbulent kinetic energy. μ_t represents eddy viscosity.

$C_{1\varepsilon}$, $C_{2\varepsilon}$, C_μ, σ_k and σ are model constants and take the values. The values of model constants are also different for different models. The realizable $k-\varepsilon$ model (high-Re) (Shih *et al.* (1995)) was used for modeling the turbulence flow. The realizable $k-\varepsilon$ model contains a new formulation for the turbulent viscosity and a new transport equation for the dissipation rate, ε, that is derived from an exact equation for the transport of the mean-square vorticity fluctuation. It introduces a variable C_μ instead of a constant. Better performance in flows that involve rotation, boundary layers under strong adverse pressure

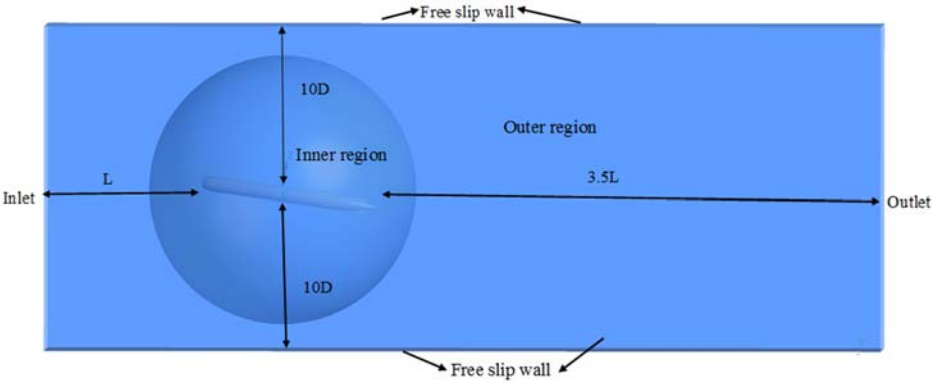

Fig. 2. The designed model for flow simulation.

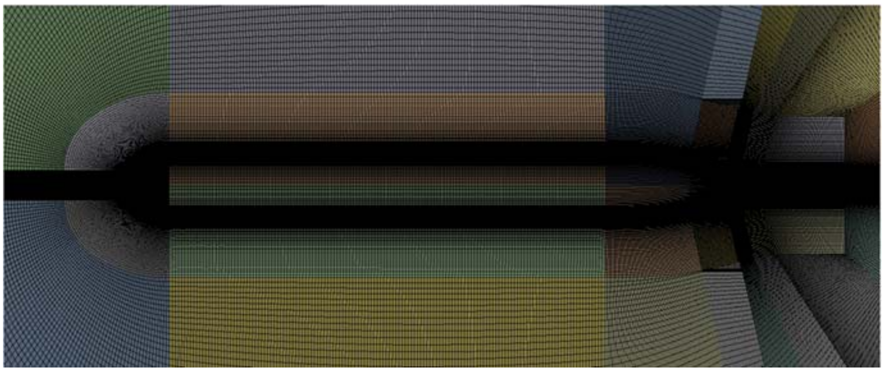

Fig. 3. Meshing around the model body.

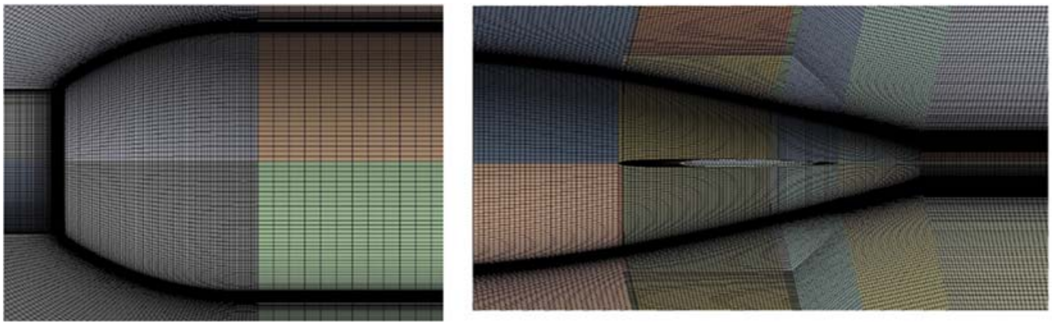

Fig. 3. Meshing around the model body.

gradient, flow separation, and re-circulating flows are enumerated as advantages of the realizable $k-\varepsilon$. As to the dynamic updating ability of viscosity and the modified transport equation for ε, the realizable $k-\varepsilon$ can effectively model all the effects of the boundary layer including the close to wall phenomenon.

3.2 Geometrical Modeling and Boundary Conditions

In the solving context, the model is located under a different AOA relative to the flow, and the flow is solved in various Reynolds. To save time, the whole grid is planned before starting meshing. Figure 2 shows the designed model for meshing and producing various AOAs. To develop various AOAs, the computational domain is divided into two outer and inner regions. The HydroLab 500 is located in the inner region, which is sphere shaped. The computational domain collection is cube shaped. To create a different AOA relative to the flow, the inner region rotates against the outer region. This rotation is imposed on the sphere. Figure 2 shows the dimensions of the solution domain of fluid. The boundary conditions are imposed to the outer region and the HydroLab 500 body. The velocity inlet boundary condition and the pressure outlet are imposed on the inlet and outlet boundaries. A no-slip condition is imposed on the surface of the body. The zero normal velocity gradient (free slip wall) is applied to the upper-lower and side surfaces.

3.3 Meshing and Grid Independence

In this study, a structured grid with hexahedral cells was applied to all areas. Results from the numerical study highly depended on the meshing parameters. Figure 3 illustrates meshing around the body. Nodes around the whole AUV are distributed along the

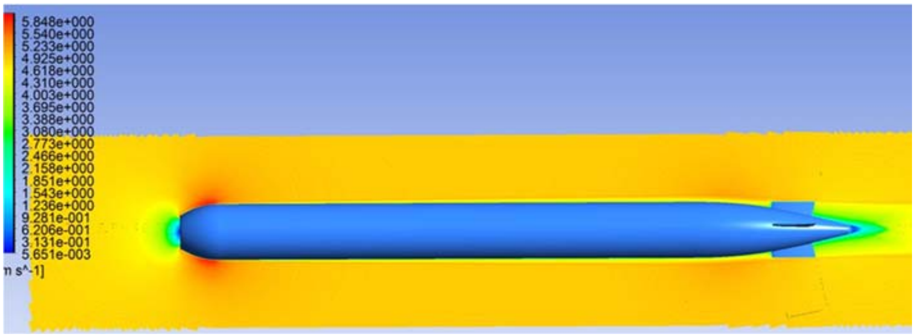

Fig. 4. Contour plot of the velocity field at zero degree of angle of attack.

hull, so that the flow close to the body is better resolved. Figure 4 shows meshing around the nose and wings. At the end of AUV, due to the formation of recirculating flows and a wake, the cells are more compressible. Due to the complication of flow around wings, meshing is done here with higher accuracy. Skewness refers to the shape difference of cells with an equilateral cell in the equivalent volume. The most difficult region for reducing skewness is the region where there are wings. Near the body wall and the wings, the skewness is not over 0.56. This can be satisfying. Going away from the wall, the mean skewness reduces.

Before analysing CFD, solving sensitivity to the grid should be considered. Accordingly, four grids were generated to study the independence from the meshing for all of the Reynolds numbers. For example, Table 1 lists the meshing details used to study the dependency of the solution to the grid in $\mathrm{Re}=2\times10^6$. Grid 1 is chosen as the initial grid. Grids for the inner region were refined using the ratio of $\sqrt{2}$ in each direction toward the previous grid (ITTC quality manual (1999)). The refinement ratio for outer region was less than $\sqrt{2}$. The meshing number varied between 0.874 and 11,892 million grid. y^+ was the non-dimensional distance of the first node near to the wall, which related to the accuracy of the numerical predication. For a realizable $k-\varepsilon$ model with standard wall function, y^+ between 30 and 300 was required. Here, y^+ varies from 30 for the finest grid to 80 for the coarsest one. The convergence test was conducted with a concentration over force and moment coefficients' imposing on the body at an angle of 0 and 10 degrees. The available commercial CFD solver FLUENT was used in the current work to conduct numerical simulations. The SIMPLE algorithm was used for pressure-velocity coupling. A second order upwind scheme was applied for discretization of momentum, turbulence kinetic energy and a turbulence dissipation rate in all the computations (Patankar *et al.* (1980)). The convergence criteria were set as 10^{-6} for all the residues. No significant difference was observed for the drag and lift coefficient in grids 3 and 4. Considering the calculation cost, therefore, grid 3 was selected for the calculations.

Table 1 Sensitivity of hydrodynamic parameters to grid size changes

AOA($^\circ$)	Grid size (million)	y^+	C_D	C_L
0	0.874	80	0.19227	0.00192
0	2.153	56	0.18361	0.00048
0	5.248	40	0.18073	0.00015
0	11.892	30	0.17988	0.00017
10	0.874	80	0.27501	0.42337
10	2.153	56	0.26346	0.41299
10	5.248	40	0.26036	0.40908
10	11.892	30	0.25971	0.40821

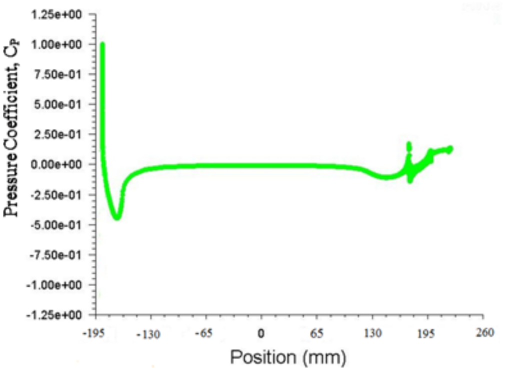

Fig. 5. Variation of pressure coefficient around AUV at zero degree of angle of attack.

Figure 4 shows the attached flow at zero degree of angle of attack. In the AUV head zone a velocity increase also can be seen which results from the AUV movement and incompressibility of the water. It is possible to the wake after the main body. The pressure coefficient, C_P around the hull is shown in Fig. 5. At first, the value of pressure coefficient decreases near the leading edge after which it increases and becomes constant around the parallel middle body. Near after body the curve dips for a while and then moves up.

4. VALIDATION

To validate the CFD results, several experimental tests were done on HydroLab 500 in $\mathrm{Re}=2\times10^6$ in the water tunnel. Figure 7 shows the set-ups for doing the experimental runs. The model AOA varied relative to the flow, using the angle adjustor located on the water tunnel. Forces and moments were measured by a 6-component strain gauge balance (Nouri *et al.* (2014)) located in the HydroLab 500 model. Tests were done at an attach angle from -4 to 6 degree with an increment of 2°. Figure 8 shows the non-dimensional normal force, Z', against the non-dimensional transverse velocity, w', for two experimental and numerical methods. The non-dimensional pitch moment, M', against w' around the volume center is depicted for both methods in Fig. 9. For small angles, there was a good agreement between the numerical and the experimental data. The difference between the numerical and experimental data increased with the AOA increment. This increase could be the result of the effect of sting on the flow at the end of HydroLab 500. Table 2 lists the hydrodynamic derivative values obtained by curve fitting Equations (4) and (5) for the numerical and experimental data. $Z_{w'|w'|}$ and $M'_{w'|w'|}$ obtained by the experiment tests were greater than the values estimated by numerical simulation data. Increased nonlinear effects can have been a result of the nonlinear effects of the sting rod on the AUV flow. The maximum derivative difference estimated from the numerical model by experimental tests was 7,5%.

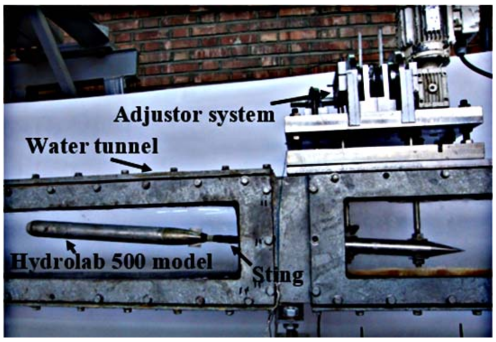

Fig. 7. Experimental set-up in the water tunnel.

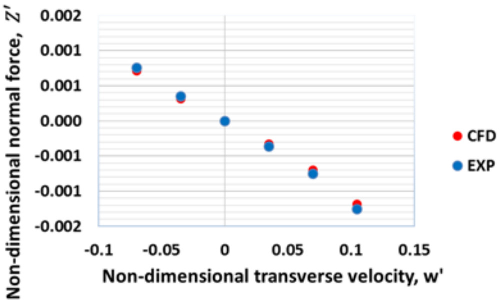

Fig. 8. Comparison of the non-dimensional normal force estimated by the experimental and numerical methods.

5. RESULTS AND DISCUSSION

To study the Reynolds effect on the hydrodynamic characteristics of HydroLab 500, flow for Reynolds numbers between 2×10^6 and 150×10^6 was solved in various AOAs. By a 2-degree increase, the HydroLab 500 AOA in the numerical model varied from -10 and 10.

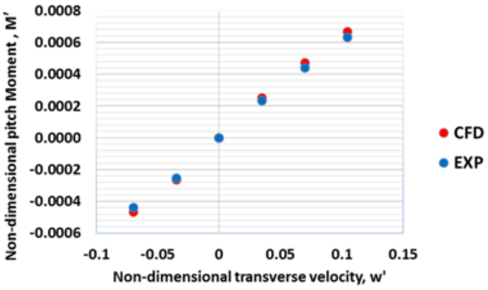

Fig. 9. Comparison of the non-dimensional pitch moment estimated by the experimental and numerical methods.

Table 2 Comparison of the hydrodynamic derivatives estimated by both numerical and empirical methods

Coefficients	Hydolab 500 (CFD)	Hydolab 500 (EXP)	Error (%)
$Z'_{w'}$	-0.0102462	-0.010962	6.5
$M'_{w'}$	0.005374	0.005651	5.0
$Z'_{w'\|w'\|}$	-0.009473	-0.009983	5.1
$M'_{w'\|w'\|}$	-0.003071	-0.003310	7.3

5.1 Study of Reynolds Effect on Drag, Lift, and Moment Coefficients

Figure 10 shows the drag coefficients for AOA= 0°, 2°, 4°, 6°, 8°, and 10° against the Reynolds number. For all AOAs, when the Reynolds number increases, the drag coefficient decreases and inclines toward a constant in the limit state.

Figure 11 shows the differentiated values of the total drag coefficient as pressure and friction drag against the Reynolds number. Results showed that pressure drag coefficient will have insignificant changes at a small angle (AOA≤4°) because of a lack of boundary layer separation. C_{Dp} increases with the Reynolds number at greater angles (AOA>4°) because of boundary layer separation in the end body. At small angles of attack, the friction drag coefficient decreases with an increase in the Reynolds number and inclines toward a constant limit state. When Reynolds numbers are high, the boundary layer is thin, and the effects of roughness enter the outer region. This causes elimination of the sub-layer. The condition of complete roughness makes the friction coefficient independent of the Reynolds number and the roughness geometry. In general, the drag coefficient at a higher Reynolds number is less sensitive to the angle increases because it is more affected by the pressure distribution. The main reason for this behavior of

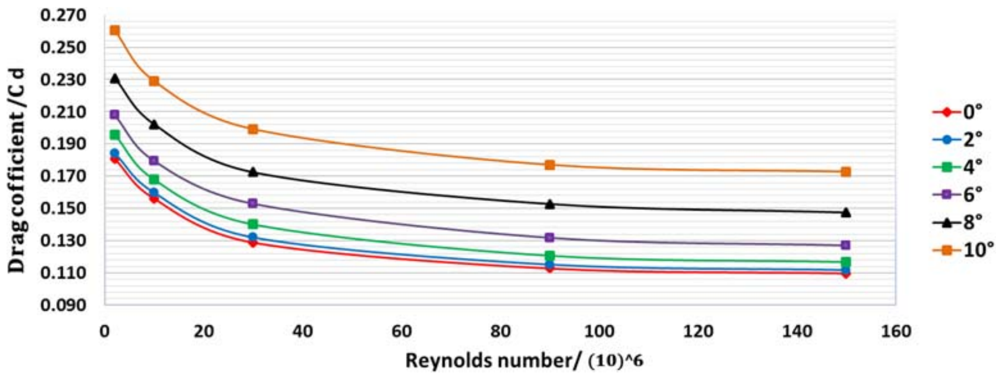

Fig. 10. The effect of Reynolds number on the drag coefficient in different AOA.

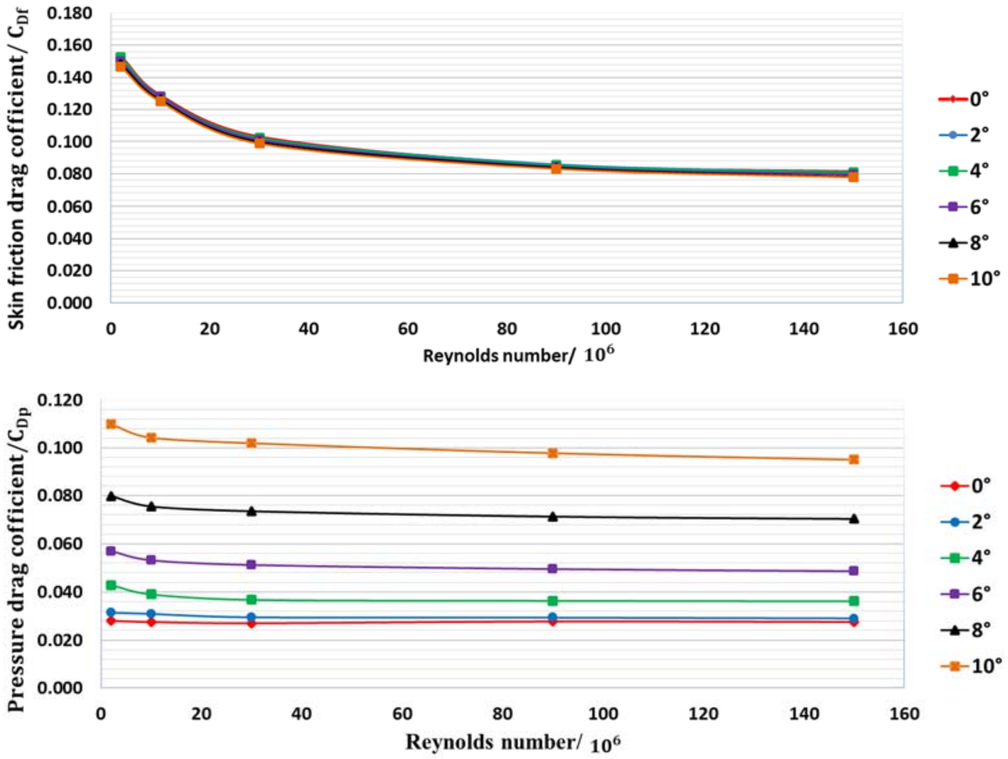

Fig. 11. Effect of Reynolds number on pressure and friction drag coefficients in different AOAs.

C_D is, as the angle of attack increases, C_{Dp} increases, but C_{Df} shows only a little change.

The lift coefficient based on the Reynolds number at angles of AOA= 0°, 2°, 4°, 6°, 8°, and 10° is depicted in Fig. 12. The results show that at smaller angles, lift coefficient partly depends on the Reynolds number. Due to a lack of separation boundary over the surface at small angles, the lift coefficient relates to the pressure distribution that results from the object geometry. At bigger angles, dependence on the Reynolds number is observed because of the relocation of the separation point.

When the Reynolds number ($Re<30\times10^6$) is small, the flow is more affected by positive pressure gradients. As a result, the Reynolds number in a smaller range affects the lift coefficient more. The variation of the moment coefficient for AOA= 0°, 2°, 4°, 6°, 8°, and 10° based on the Reynolds number is shown in Fig. 13. For all AOAs, when the Reynolds number increases, the moment coefficient increases and inclines toward a constant value in the limit state. With an increased AOA, C_M is more affected by the Re numbers.

5.2 Effect of the Reynolds Number on Hydrodynamic Derivatives

Figure 14 shows the non-dimensional values of the normal forces and pitch moments based on the AOAs for different Reynolds numbers. At angles of attack under 4°, increasing the Reynolds number does not produce any significant change in Z' and M'. At angles larger than 6°, increasing the Reynolds number decreases Z' and increases M'. Combined effects derived from increased AOAs and the relocation of the center of the pressure increases M'.

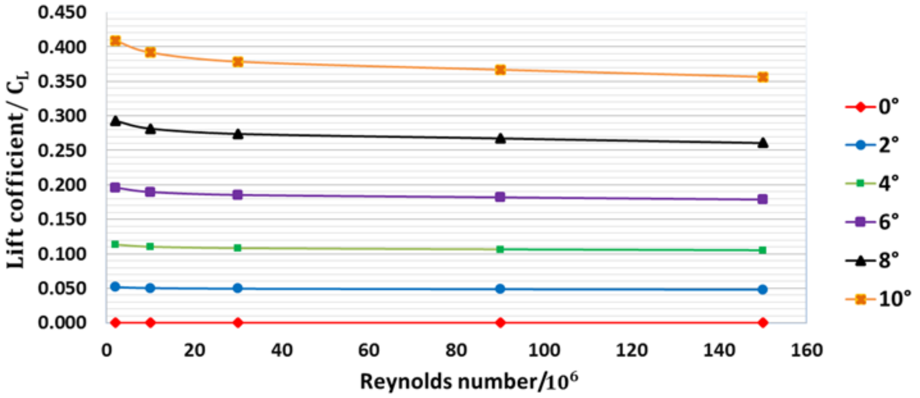

Fig. 12. Effect of Reynolds number on lift coefficients in different AOAs.

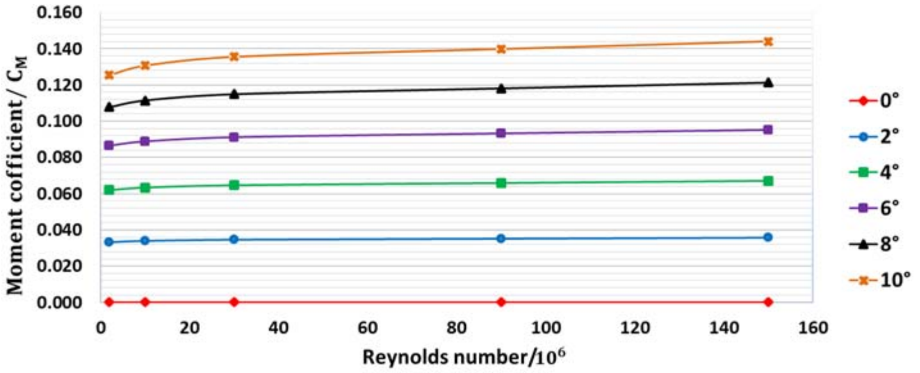

Fig. 13. Effect of Reynolds number on moment coefficients in different AOAs.

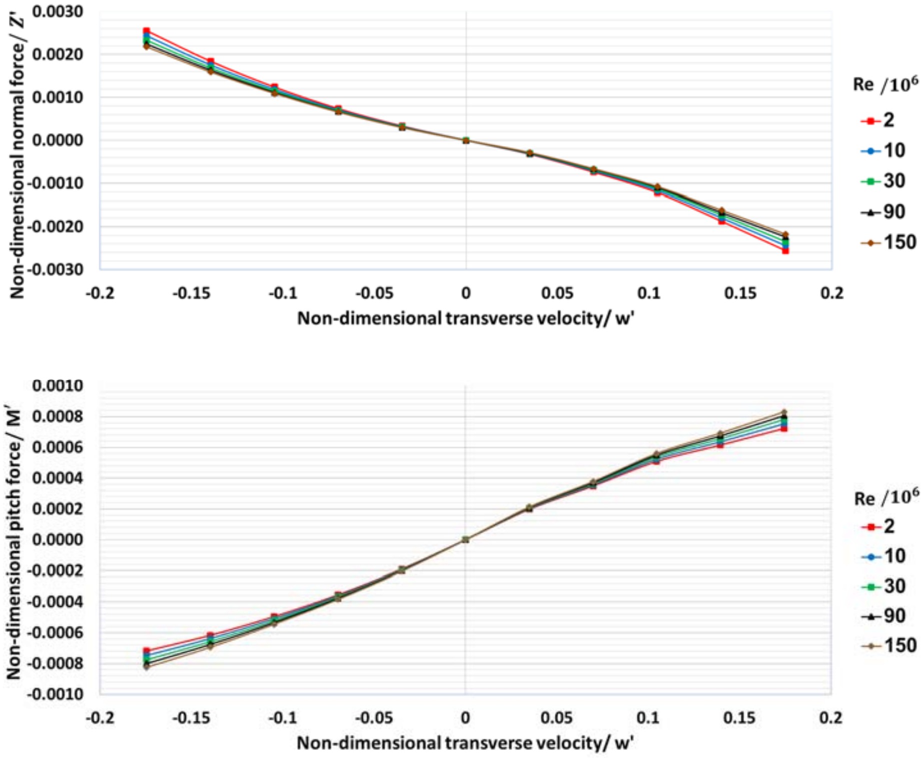

Fig. 14. Non-dimensional values of normal forces and pitch moments based on AOAs for different Reynolds numbers.

The value of all types of maneuver coefficients in equations (5) and (6) can be estimated by data regression. The linear components $Z_{w'}$ and $M_{w'}$ are defined as the effects of potential flow and

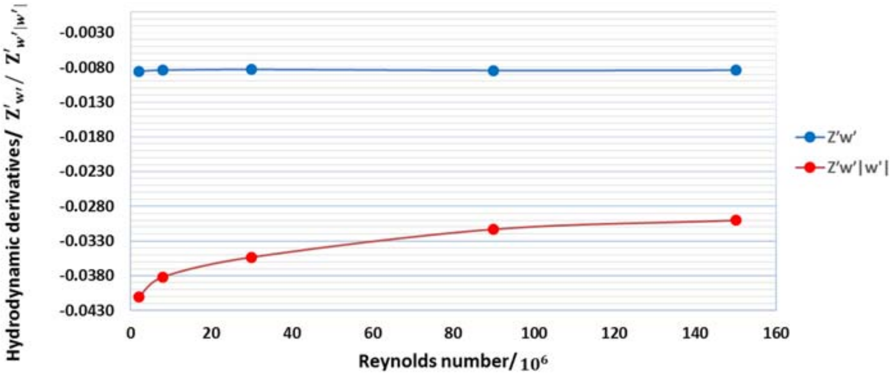

Fig. 15. Derivatives related to normal forces based on the Reynolds number.

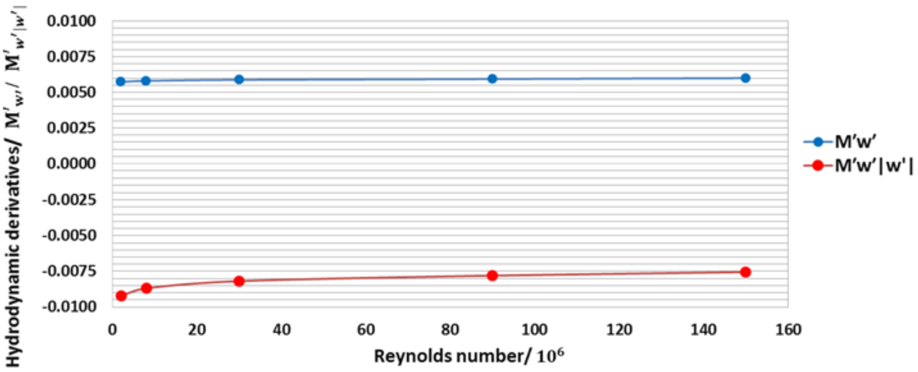

Fig. 16. Derivatives related to pitch moments based on Reynolds numbers.

$Z_{w'|w'|}$ and $M_{w'|w'|}$ are defined as the viscous effects. Figures 15 and 16 show the linear and nonlinear derivative values that relate to the normal force and pitch moment based on the Reynolds number. In Figs 15 and 16, an increased Reynolds number decreases the absolute values of the linear coefficients. This finding can be due to the effects of object separation. $Z_{w'|w'|}$ and $M_{w'|w'|}$ show the cross drag due to the viscous effect of the flow.

The cross drag can be affected by the effects of the turbulence boundary layer, shedding of vortex sheets, and the separation phenomenon. $Z_{w'|w'|}$ and $M_{w'|w'|}$ decrease when the Reynolds number increases and inclines toward a constant limit state. At a high Reynolds number, the roughness heights located in the outer region make the separation point and the vertical flow independent of the roughness geometry and the Reynolds number. Therefore, it can be concluded that with an infinite Reynolds number, the induced nonlinear effects converge on a constant value.

The stability linearity derivatives were estimated by data related to small angles (AOA<4°). In Tables 3 and 4, the estimated values for the linear derivatives are compared, using data under 4° and whole data (maneuvering derivatives). Values obtained by these values show that increased Reynolds numbers produce trivial changes. This may be a consequence of the independence of the potential flow of the Reynolds number. Comparing the results of linear derivatives shows that increased Reynolds numbers decrease the difference in the values.

Table 3 Comparing the stability and maneuvering linear derivatives related to normal force

Reynolds Number, Re × 10^6	Stability Derivatives	Maneuvering Derivatives
2	-0.0106606	-0.00853
10	-0.01023364	-0.00818
30	-0.00990214	-0.00829
90	-0.00964559	-0.00843
150	-0.0095157	-0.00842

Table 4 Comparing stability and maneuvering linear derivatives related to pitch moment

Reynolds Number, Re × 10^6	Stability Derivatives	Maneuvering Derivatives
2	0.005002	0.0057286
10	0.005114	0.0058023
30	0.005219	0.0058736
90	0.005318	0.0059301
150	0.005414	0.0059919

6. CONCLUSION

This paper evaluates the effects of Reynolds number on drag and lift coefficients and linear and nonlinear derivatives at different AOAs using a numerical model. The presented model was validated by experimental tests in the water tunnel. The physical factors that affected the results were identified, and their effects were analyzed using estimated parameters. The results show that some hydrodynamic parameters can be a function of Re, so that they converge on a limited state by increasing the Reynolds number to a constant. The parameter independence of Re relies on the type of parameter and the AOA of the AUV. The proposed model can be employed to estimate the hydrodynamic features related to AUVs. These results are useful for designing better optimal geometry, the control system, and steering of similar AUVs for operational conditions.

REFERENCES

Barros, E. A., L. D. Dantas, A. M. Pascoal and S. A. Ede (2008). Investigation of Normal Force and Moment Coefficients for an AUV at Nonlinear Angle of Attack and Sideslip Range. *Journal of Oceanic Engineering 33*, 583-579.

Bellevre, D., D. Diaz, A. Tuesta and P. Perdon (2001). Submarine Maneuverability Assessment Using Computational Fluid Dynamic Tools. *In Twenty-Third Symposium on Naval Hydrodynamics* 820-832, Val de Reuil, France.

Du, X. X., H. Wang, C. Z. Hao and X. L. Li (2014). Analysis of hydrodynamic characteristics of unmanned underwater vehicle moving close to the sea bottom. *Defence Technology* 10(1), 76-81.

Husaini, M., Z. Samad and M. R. Arshad (2009). CFD Simulation Of Cooperative AUV Motiandon, *Indian Journal of Marine Sciences* 38, 346-351.

Jagadeesh, P. (2011). RANS prediction for drag characteristics over cooperative axisymmetric bodies. *International Journal of Earth Sciences and Engineering* 4, 628-631.

Jagadeesh, P., K. Murali and V. G. Idichandy (2009). Experimental investigation of hydrodynamic force coefficients over AUV hull form. *Ocean Engineering* 36(1), 113-118.

Kim, H. and H. Cho (2011). Numerical study on control derivatives of a high-speed underwater vehicle. *Journal of mechanical science and technology* 25(3), 759-765.

Mansoorzadeh, S. and E. Javanmard (2014). An investigation of free surface effects on drag and lift coefficients of an autonomous underwater vehicle (AUV) using computational and experimental fluid dynamics methods. *Journal of Fluids and Structures* 51, 161-171.

Manual, I. Q. (1999). *Uncertainty Analysis in CFD and Guidelines for RANS codes*, 22nd ITTC.

Nouri, N. M., K. Mostafapour, M. Kamran and R. Bohadori (2014). Design methodology of a six-component balance for measuring forces and moments in water tunnel tests. *Measurement* 58, 544-555.

Patankar, S. (1980). Numerical heat transfer and fluid flow. *CRC press*.

Phillips, A. B., M. Furlong and S. R. Turnock (2007). The use of computational fluid dynamics to determine the dynamic stability of an autonomous underwater vehicle, *in Proceedings of 10th Numerical Towing Tank Symposium*, Hamburg, Germany.

Rattanasiri, P., P. A. Wilson and A. B. Phillips (2014). Simple drag prediction strategies for an Autonomous Underwater Vehicle's hull shape. *USYS14*.

Sarkar, T., P. G. Sayer and S. M. Fraser (1997). A study of autonomous underwater vehicle hull forms using computational fluid dynamics. *International Journal for Numerical Methods in Fluids* 25(11), 1301-1313.

Shih, T. H., W. W. Liou, A. Shabbir, Z. Yang and J. Zhu (1995). A new k-ε eddy viscosity model for high reynolds number turbulent flows. *Computers & Fluids* 24(3), 227-238.

Tyagi, A. and D. Sen (2006). Calculation of transverse hydrodynamic coefficients using computational fluid dynamic approach. *Ocean Engineering* 33(5), 798-809.

Wu, B. S., F. Xing, X. F. Kuang and Q. M. Miao (2005). Investigation of hydrodynamic characteristics of submarine moving close to the sea bottom with CFD methods. *Journal of Ship Mechanics* 9(3), 19-28.

Zhang, H., Y. R. Xu and H. P. Cai (2010). Using CFD software to calculate hydrodynamic coefficients. *Journal of Marine Science and Application* 9(2), 149-155.